Evaluation of Microhole Drilling Technology for Geothermal Exploration, Assessment, And Monitoring

SAND2021-7485 C

Jiann-Cherng Su[1], Anirban Mazumdar[2], Stephen Buerger[1], Adam Foris[1],

and Brian Faircloth[3]

[1]Sandia National Laboratories

[2]George W. Woodruff School of Mechanical Engineering, Georgia Institute of Technology

[3]Foro Energy, Inc.

Keywords: *Geothermal, Microholes, Slimholes, Drilling, Exploration, Monitoring*

ABSTRACT

The well documented promise of microholes has not yet matched expectations. A fundamental issue is that delivering high weight-on-bit (WOB), high torque rotational horsepower to a conventional drill bit does not scale down to the hole sizes necessary to realize the envisioned cost savings. Prior work has focused on miniaturizing the various systems used in conventional drilling technologies, such as motors, steering systems, mud handling and logging tools, and coiled tubing drilling units. As smaller diameters are targeted for these low WOB drilling technologies, several associated sets of challenges arise. For example, energy transfer efficiency in small diameter percussive hammers is different than conventional hammers. Finding adequate methods of generating rotation at the bit are also more difficult.

A low weight-on-bit microhole drilling system was proposed, conceived, and tested on a limited scale. The utility of a microhole was quantified using flow analyses to establish bounds for usable microholes. Two low weight-on-bit rock reduction techniques were evaluated and developed, including a low technology readiness level concept in the laser-assisted mechanical drill and a modified commercial percussive hammer. Supporting equipment, including downhole rotation and a drill string twist reaction tool, were developed to enable wireline deployment of a drilling assembly. Although the various subsystems were tested and shown to work well individually in a laboratory environment, there is still room for improvement before the microhole drilling system is ready to be deployed. Ruggedizing the various components will be key, as well as having additional capacity in a conveyance system to provide additional capacity for pullback and deployment.

Introduction

One of the greatest barriers to widespread geothermal energy development is the high cost of drilling during exploration, assessment, and monitoring. Albright and Dreesen (2003) suggest that microhole drilling—small diameter boreholes under 4 in. (10 cm)—could reduce costs by up to 70% over conventional drilling. Zhu et al. (1995) suggest that microhole drilling could reduce costs by 40–60% for exploration wells and 25–40% for production and injection wells compared to conventional (large diameter) drilling techniques. However, microhole drilling technology has not lived up to expectations, primarily because delivering high weight-on-bit (WOB), high torque rotational horsepower to a conventional drill bit does not easily scale down to the smaller diameter boreholes necessary to realize the cost savings.

Previous work has focused on miniaturizing the systems used in conventional drilling technologies (Jeanloz and Stone, 2013), and although notable gains were made in those efforts, high WOB drilling technologies were relied upon at the rock/bit interface. Unfortunately, problems with drill string loading, such as buckling, friction, and twist, become more severe as the borehole diameter decreases.

The notion of drilling smaller diameter boreholes has existed since the 1950s when efforts at slimhole drilling and miniaturization were investigated for oil exploration (Randolph et al., 1991; Albright and Dreesen, 2000). Previous microhole studies (Jeanloz and Stone, 2013; National Energy Technology Laboratory, 2006) have focused on high WOB drilling technologies, which deliver high torque rotational horsepower to a conventional drill bit but unfortunately, do not easily scale down to smaller diameter boreholes. Research at Los Alamos National Laboratory (Albright and Dreesen, 2005) demonstrated the feasibility of drilling microholes to intermediate depths (~800 ft [~244 m]) using mechanical rotary bits and a hydraulically powered positive displacement motor.

Our research focused on implementing and evaluating two low WOB drilling technologies for microhole drilling:

- Laser-assisted mechanical drill, which we tested in the laboratory and
- Lightly modified commercial off-the-shelf (COTS) percussive hammer, which was tested in a limited field test.

We designed, built, and tested each drilling system; evaluated options for downhole bit rotation; and developed a novel mechanism for effective and controllable downhole WOB transmission and torque reaction. Although we demonstrated the technical feasibility of the overall system, we also identified several areas for further investigation and improvement, particularly in the areas of durability, manufacturability, and reliability.

Flow Simulations

First, we conducted a parametric study to determine the limiting flow rate as a function of borehole depth, borehole diameter, enthalpy, productivity index (PI), and flow rate. This was done to bound the size of usable microholes. Two hypothetical microholes were used in the simulations, one at a depth of 3,000 ft (914 m) and one at a depth of 6,000 ft (1,829 m). Borehole diameter ranged from 1.8 in.–5.0 in. (4.6–12.7 cm), productivity index (PI) ranged from 2.1–25 TPH/bar (0.3–4.0 MTPH/psi), and enthalpy ranged from 814–2,791 kJ/kg (350–1,200 BTU/lbm). For each simulation, a choke rate was determined for combinations of borehole diameter, PI, and enthalpy. Choke rate represents the flow rate at which the well will no longer sustain flow. Smaller diameter boreholes experience choked conditions at lower flow rates and have lower maximum flow for any given enthalpy. Generally, fluids with relatively high or low enthalpy will choke at lower maximum rates than moderate enthalpy wells.

Isosurfaces were constructed at arbitrary and regularly spaced intervals between 23 and 113 TPH (50 to 250 MTPH) to represent the conditions under which choked flow occurs (see Figure 1 through Figure 4). The red squares represent individual borehole simulations. Points to the left (or above and below) each isosurface represent conditions under which the well is choked and will not flow, while points to the right (or within) the isosurface represent flowing conditions. Isosurfaces for smaller diameter boreholes showed less variation in PI—indicated by the leading edge of the isosurface being nearly parallel to the PI axis—while larger borehole diameters showed appreciable variation in PI (Figure 1). This is because friction pressure becomes the dominant variable at smaller borehole diameters. Flowing conditions in these small diameter boreholes are not sensitive to PI, and the test results are not useful for scaling borehole performance to larger borehole diameters because the indicated PI yields a nonunique solution.

For larger bottom hole diameters, there is significant sensitivity to PI. Borehole diameter and enthalpy data pairs located to the right of an isosurface have enough variability in PI to allow unique solutions when scaling up borehole performance to larger diameters. Figure 2, which includes only the data points for enthalpy of 1,744 kJ/kg (750 BTU/lbm), shows the progressive increase in PI variability from smaller to larger borehole sizes.

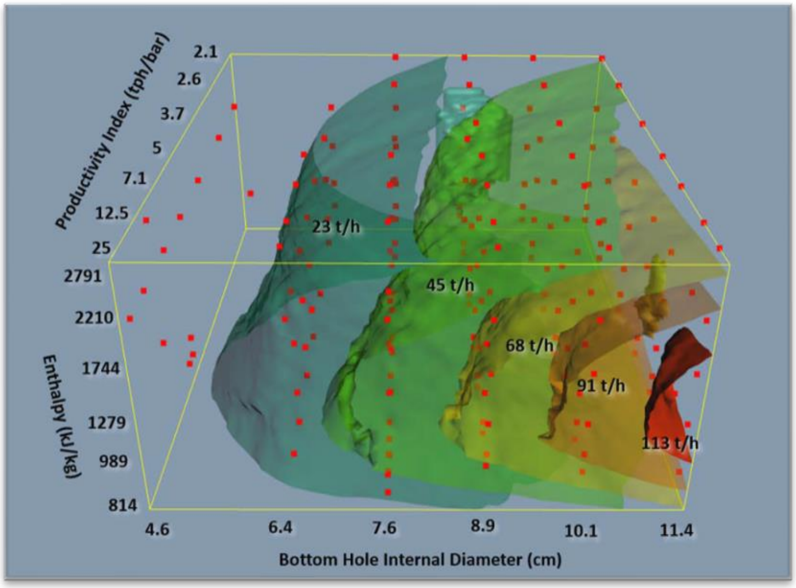

Figure 1: Choke rate in a 914 m (3,000 ft) borehole based on simulated variation in borehole size (x-axis), PI (y-axis), and enthalpy (z-axis).

Figure 2 illustrates the sensitivity to enthalpy and borehole diameter. Figure 3 shows the sensitivity of the isosurfaces to enthalpy and demonstrates that moderate enthalpy fluids can sustain flow in much smaller boreholes, whereas cooler lower enthalpy fluids do not have sufficient energy to overcome friction pressure and higher flash enthalpies choke due to expanded volume.

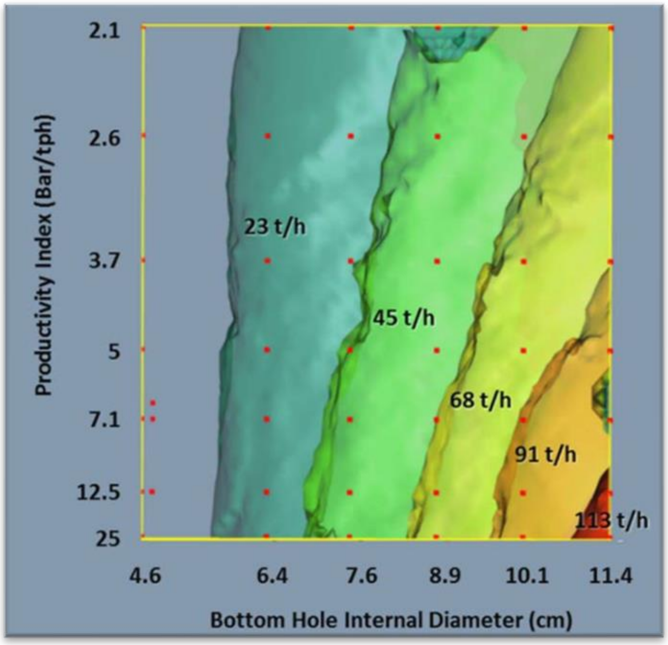

Figure 2: Simulations for 914 m (3,000 ft) borehole: choke rate as a function of PI and borehole diameter for a range of flow rates with a flowing enthalpy of 1,744 kJ/kg (750 BTU/lbm).

In Figure 3 the isosurfaces shown in Figure 1 are rotated so the effects of borehole size and enthalpy are more prominent. (Note that the light green on the back isosurface is an artifact of contouring). In smaller boreholes, enthalpy has a slightly greater impact on flow rate with a flattening of the isosurfaces relative to the larger borehole sizes. The effect is greater for lower enthalpy than higher enthalpy. Moderate enthalpy wells with two-phase flow experienced choked flow at high flow rates and are more likely to be successfully flow-tested by smaller boreholes.

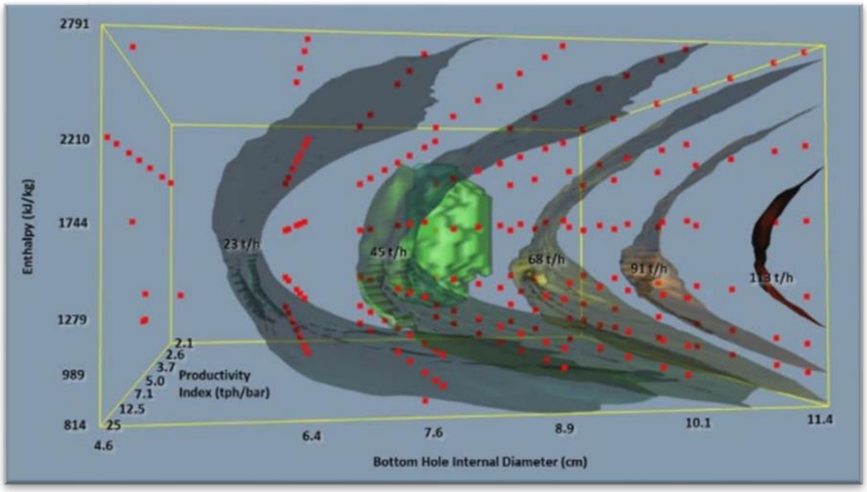

Figure 3: Simulation 914 m (3,000 ft) borehole: choke rates based on simulated variation in hole size (x-axis), PI (y-axis) and enthalpy (z-axis). (Light green on back surface is an artifact of contouring).

The analysis was repeated for an 1,829 m (6,000 ft) borehole. Boreholes sizes ranging from 4.6 cm to 7.6 cm (1.8 in. to 3.5 in.) showed negligible variation in PI at lower flow rates (Figure 4), indicating flow test parameters for these borehole sizes are not useful for scaling up to larger diameter wells. For this depth, borehole sizes should be at least 11.4 cm (4.5 in.) to allow accurate scaling to production-sized boreholes.

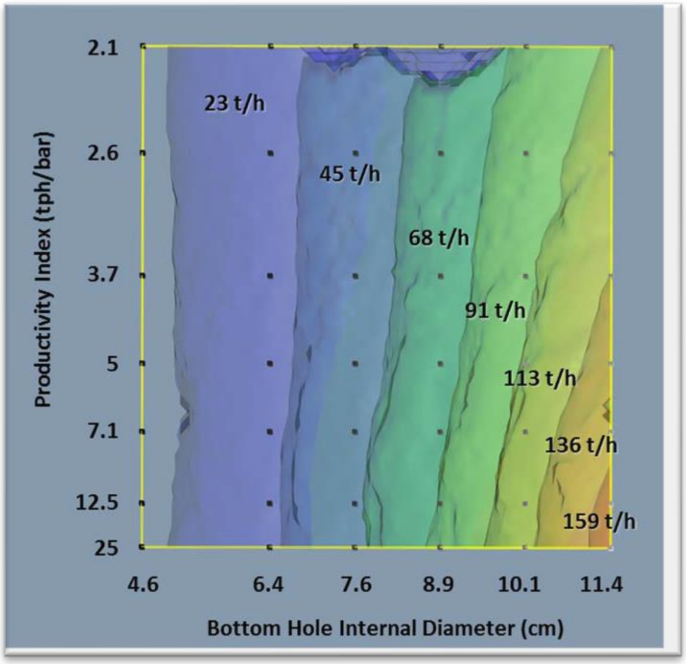

Figure 4: Isosurfaces of choked flow for an 1,829 m (6,000 ft) borehole showing choked flow as a function of PI and borehole diameter for a range of flow rates, showing sensitivity to borehole diameter and PI.

The flow simulations confirmed that microholes require an alternate method of determining PI or permeability and demonstrated that PI and injectivity index from microhole tests have limitations in scaling up to larger production-sized boreholes. It provided a bounds for defining the range of usable holes for the remainder of the project.

Laser-Assisted Mechanical Drilling

Two forms of rock reduction were considered for evaluation in this project. The first was a laser-assisted mechanical drill developed by Foro Energy as part of the overall effort. Foro designed, built, and tested a 3⅝ in. (~9.2 cm) diameter laser mechanical laboratory drilling bottom hole assembly (BHA) with extremely high laser power density. The design of the drilling assembly required water-cooling to moderate the near-bit temperature.

The laser produces cuttings through spallation and is formation dependent. To characterize the performance of the laser in the target formation (Sierra White granite), Foro calculated the threshold laser power required to cause spalling, which is critical for understanding laser/rock interactions. Equation (1) yields the maximum temperature change Sierra White granite can withstand before it fails, assuming all properties are isotropic, ν = 0.28, and fracture stress is described by the Brazilian Tensile Test (BTS).

$$\Delta \mathrm{T}_{\max} = \frac{(1-\nu)(\sigma_t + UCS)}{\alpha E} = \frac{(.72)(1280+25940)\,psi}{\left(7.56e^{-6}/{}^{\circ}C\right)\left(7.832e^{6}\,psi\right)} = 330^{\circ}C \qquad \text{Eq. 1}$$

(1)

If fracture stress is assumed to follow Equation (2) more closely than the BTS, the maximum impulse temperature rises to 356 °C (673 °F), and the fracture stress is given by equation (2).

$$\sigma_t = \frac{K_{IC}}{\sqrt{\pi C}} \qquad \text{Eq. 2}$$

Using the above calculated temperature, the laser power needed to reach minimum temperature for rock fracturing is given by Equation (3).

$$q = K\frac{\delta T}{\delta x} \rightarrow \left(2.1\frac{W}{m°C}\right)\left(\frac{330°C}{.001m}\right) = 693\frac{kW}{m^2}(.00456m^2) = 3.2kW \qquad \text{Eq. 3}$$

Experiments were performed to determine how much laser power was required to induce spalling. The laser-induced damage threshold of Sierra White was compared to Dolomite and Lake Mountain Limestone (Figure 5). The testing was performed under atmospheric conditions with a round beam diameter of 0.85 in. (~2.2 cm) and 60 scfm (1.7 m^3/min) of air through a nozzle pointed at a 45° angle to the target.

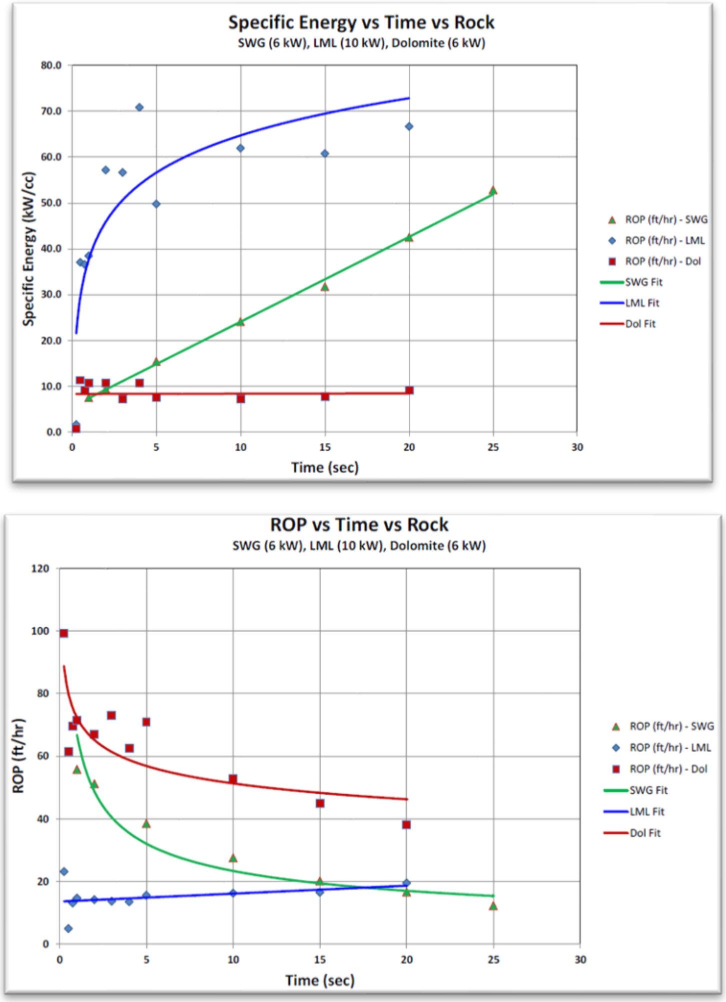

Figure 5: Specific energy vs. time vs. rock (top graph) and rate of Penetration (ROP) vs. time vs. rock (bottom graph).

Laser power is delivered to the BHA via a fiber optic cable, which has an optical connector (downhole connector) at its distal end. Beyond this is a series of optics that shape the beam into the desired bowtie configuration, and the final optic is a protective window. Spring-loaded, precisely machined spacers are used to fit the optics with minimal contact stresses to help provide alignment. Nonsymmetrical lenses were designed with flats on the outer diameter to rotationally align them to the housing. Figure 6 summarizes the performance and depicts the design.

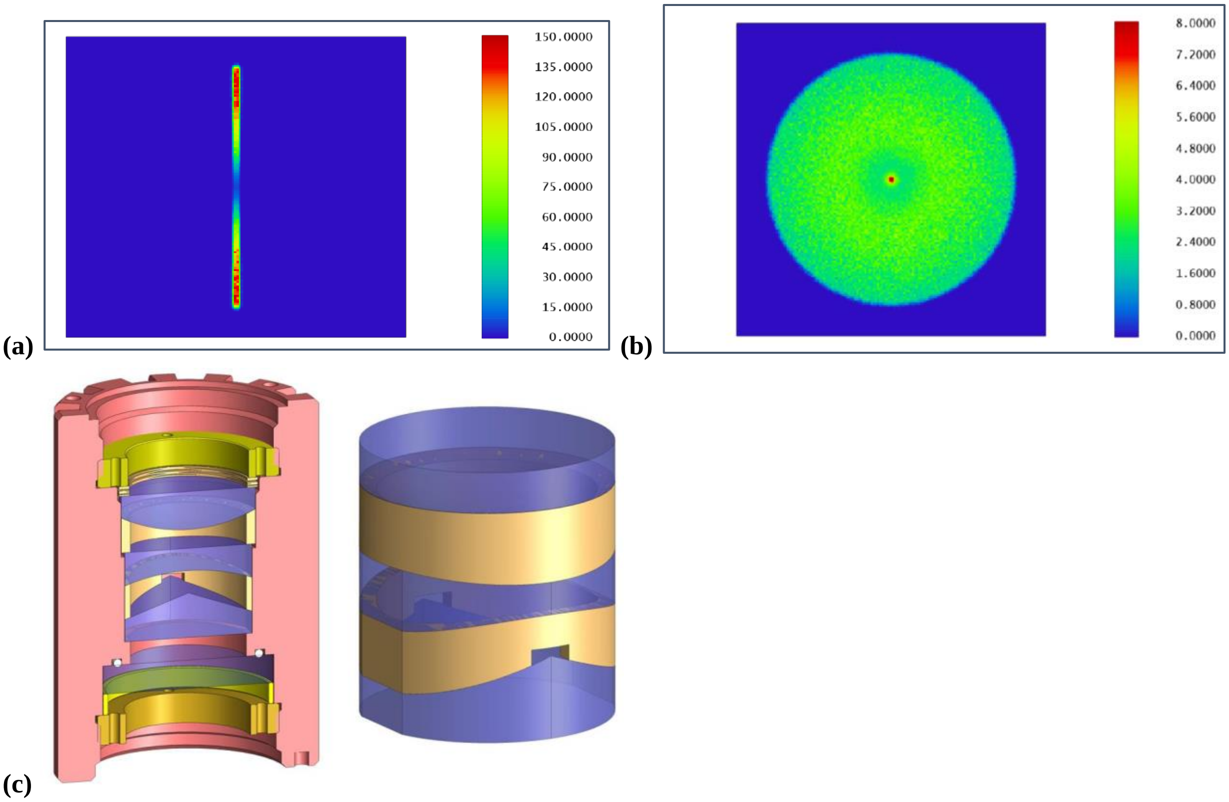

Figure 6: Instantaneous power distribution on rock surface (a); rotationally averaged laser power on rock surface (b); and optomechanical design (c).

The tool was optimized with multiple optical configurations, but we stopped optimization when reliability became an issue. The three optical configurations were a flat window, a window with a 509 mm radius concave cylinder, and a window with a 381 mm concave cylinder. The different window configurations allowed us to change the balance of laser power across the bottom of the hole. Figure 7a compares the performance of each configuration for the five different test parameters, and Figure 7b shows the assembled bit.

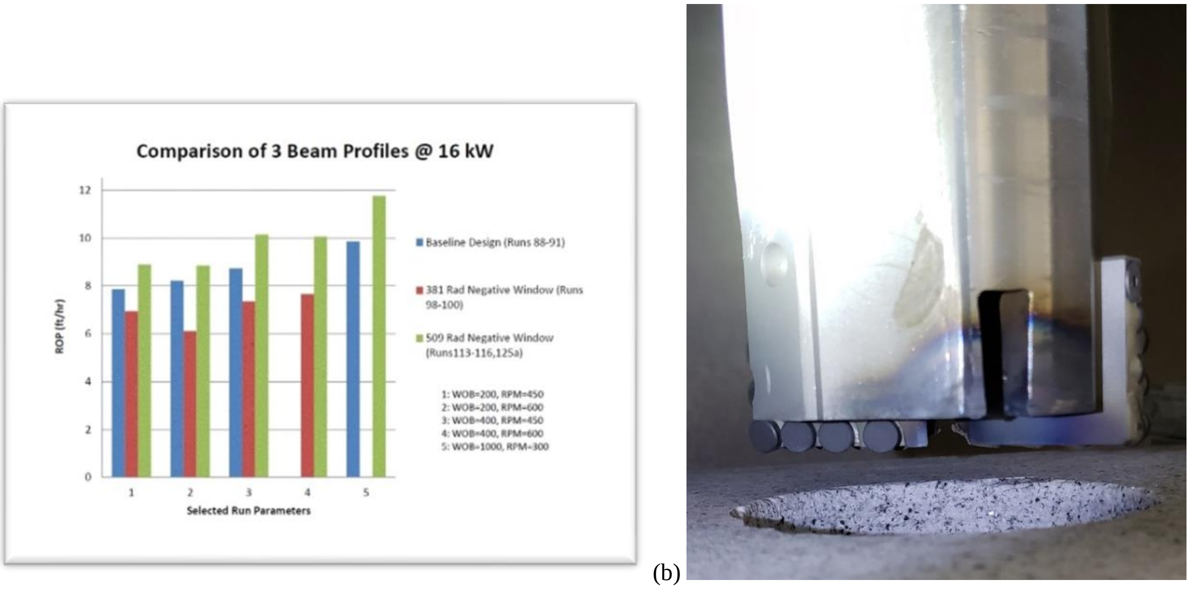

Figure 7: Comparison of different optical configurations (a) and the assembled bit (b).

The maximum rate of penetration (ROP) achieved in the laboratory was 17 ft/hr (~5 m/hr) at 1,000 lb (~454 kg) WOB, 20 kW (~27 hp) of power, and 200 rpm. The resulting torque was 70 lbf-ft (~95 Nm). Several of the observed trends were expected, such as higher laser powers resulting in higher ROP and increasing WOB increasing ROP. However, some trends were unexpected, like increasing mechanical power increasing ROP at 16 kW but not at 20 kW and higher rpm increasing ROP at 16 kW but not at 20 kW. More data is needed to verify these trends and confirm that variances between runs did not interfere with the results.

Percussive Hammer Drilling

As a complement to the laser-assisted mechanical drilling, we also pursued a more conventional approach to rock reduction to minimize overall project risk. One of the low WOB drilling technologies suitable for geothermal drilling is the percussive DTHH. Percussive hammers are an advanced and promising exploratory drilling technology for geothermal applications since they rely on rock reduction mechanisms that are well-suited for use in the hard, brittle rock characteristic of geothermal formations. DTHH are also compatible with low-density fluids that are often used for geothermal drilling. Experience in mining, as well as oil and gas drilling, has demonstrated their utility for penetrating hard rock. Percussive hammers have the potential to reduce overall well construction costs by significantly improving the penetration rates in the hot, hard, abrasive environments typical of geothermal drilling.

In a DTHH, the hammering action takes place at the end of the drill string. A fluid driven piston oscillates within an outer shell. The piston strikes the bit delivering the energy required to produce rock reduction (Figure 8). One of the primary advantages of the DTHH is that the ROP is proportional to the supplied pressure (i.e., higher pressure results in higher ROP). The limiting factor in penetration rate then becomes the durability of the hammers and bits.

Figure 8: DTHH illustration.

We explored several small diameter DTHH hammers for use on this project. The first was an Atlas Copco COP 20 DTHH (Figure 9). The COP hammers are designed for use in construction, quarrying, and exploration drilling. They operate on air pressures between 100 and 175 psi (~690 and 1,200 kPa). The hammer uses a BR2 bit shank that does not require a foot valve. The foot valve is a tubular feature that sits on the struck end of the bit. It is part of the compressed air flow path that controls the motion of the piston and is typically made from a tough plastic, such as nylon or Delrin.

Figure 9: Atlas Copco COP 20 percussive hammer.

Preliminary drilling tests were conducted using the COP 20 DTHH with a 3 in. (~7.6 cm) bit. Figure 10 assesses the performance of the small-diameter valveless foot design. The tests were conducted at the Sandia High Operating Temperature (HOT) drilling facility using an external 175 psi (~1,200 kPa) compressor. Sierra White granite, which has a published unconfined compressive strength (UCS) of 22 ksi (~150 kPa), was used for the tests.

Figure 10: Percussive hammer bit engaged with rock.

The hammer had reliability issues related to inconsistencies in piston cycling, and there were several occasions when the hammer would not operate consistently on startup. Consequently, we decided to use more mainstream hammer designs for the remainder of the percussive hammer tests. After problems were encountered with the COP 20 hammer, we consulted the factory for a better choice of DTHH for our application, and it was recommended that we use the QLX line of hammers based on the expected operating conditions. The QLX 35 (Figure 11) was chosen for its performance characteristics and size.

Figure 11: Atlas Copco QLX 35 percussive hammer.

Conventional operation of percussive hammers requires adding petroleum-based lubricants to the compressed air stream to lubricate the moving parts of the hammer. However, those lubricants break down under expected geothermal temperatures. To address the tribology challenges (friction, wear, and lubrication) we leveraged lessons learned from the previous high-temperature percussive hammer development effort. From that effort, internal components were coated with a solid lubricant to replace the injected rock oil lubricant. The key component that requires lubrication is the piston (Figure 12). Three key contact surfaces were lubricated to prevent galling—wear caused by adhesion between sliding surfaces—and premature damage (Figure 13).

Figure 12: QLX 35 uncoated piston. Sandia worked with a commercial vendor to apply the DLC solid lubricant coating to the piston. The coating is a multi-layer lubricant that protects against adhesive wear. It also reduces the surface tribo-oxidation and increases the load-carrying capacity of the contacting surface.

Figure 13: QLX 35 piston coated with DLC for solid lubrication.

Downhole Rotation

The microhole motor concept is an amalgamation of the various drive types used in drilling. It is derived from the auto indexer, developed under a previous project funded by the Department of Energy Geothermal Technology Office, and a commercial pneumatic impact wrench. The modified pneumatic torque wrench is sized to fit in the inline form factor used in a BHA. The motor consists of two primary components: a power section and a bearing section (see Figure 14). The power section consists of a pneumatic vane motor coupled with a 3-stage gear box. The bearing section consists of stacked angular contact bearings within a steel housing modified from a commercial part produced by Ditch Witch®. An internal flow passage allows the compressed air supply to drive the percussive hammer in addition to the motor.

The motor was primarily designed to operate with a percussive hammer but can be modified for use with the laser-assisted mechanical drill by adjusting the gear ratios. The free-spinning speed is 62 rpm, while the stall torque is 890 lbf-ft (~1,200 Nm). It can operate with both compressed air and foam to aid in cuttings removal.

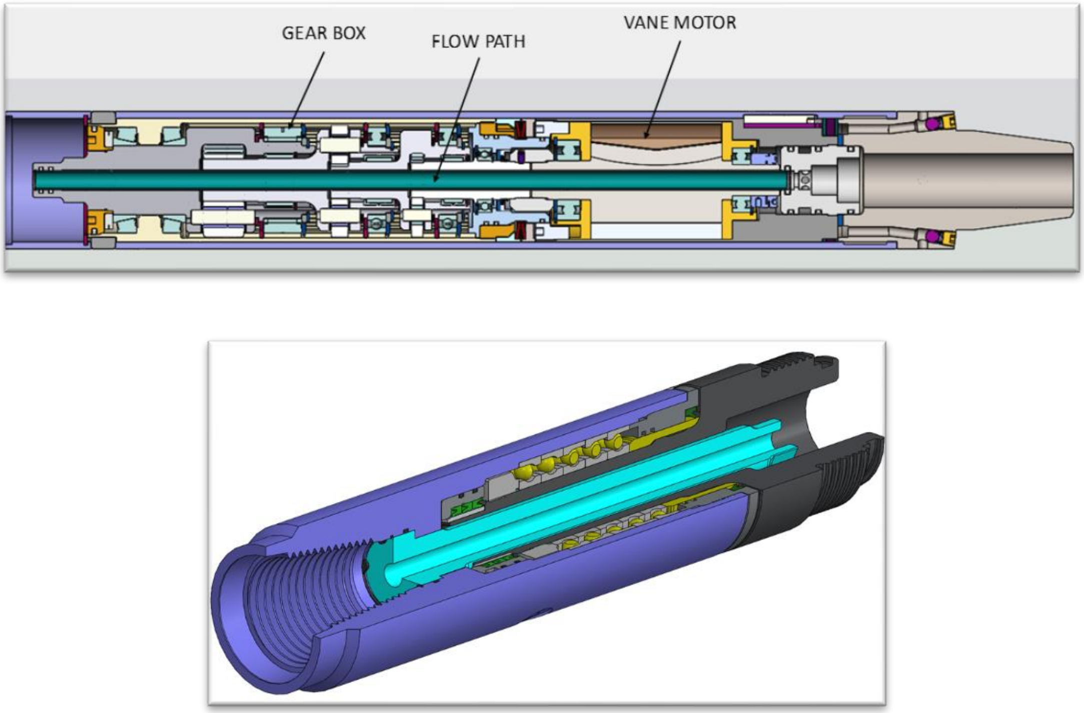

(a)

(b)

Figure 14: Cross-sections of power section (a) and bearing section (b).

The motor was tested on the Sandia Dynamometer Test Stand at two levels of inlet pressure (40 psi [~275 kPa] and 80 psi [~550 kPa]) to assess the performance of the motor under a load, and the results are shown in Figure 15. Tests were conducted until the motor was no longer able to turn the dynamometer (stall torque).

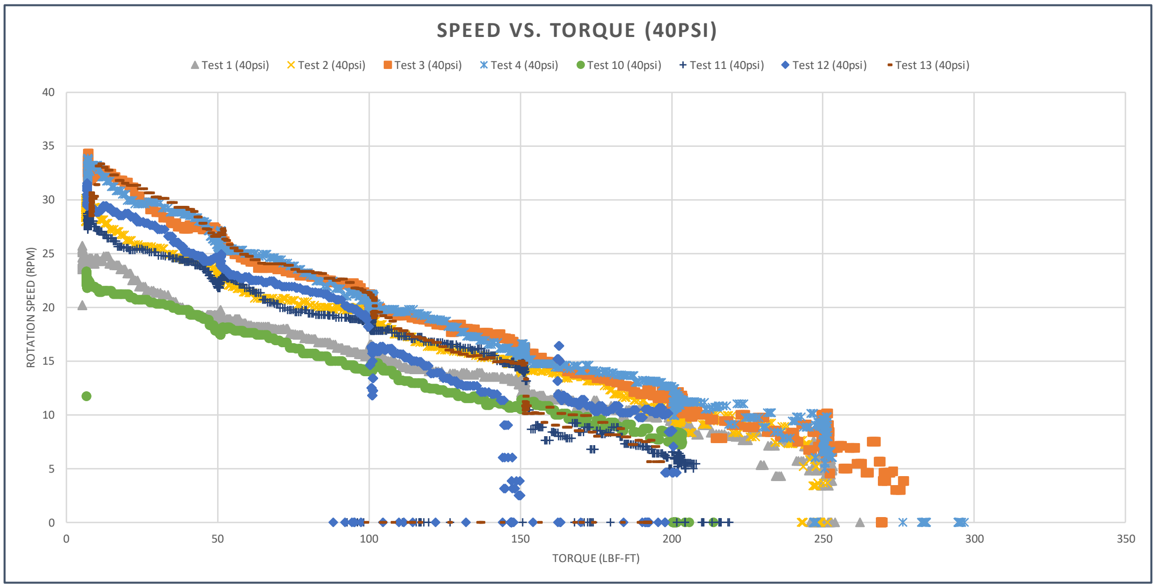

(a)

Figure 15(a): Sample dynamometer results for microhole downhole motor: 40 psi (~275 kPa) inlet pressure.

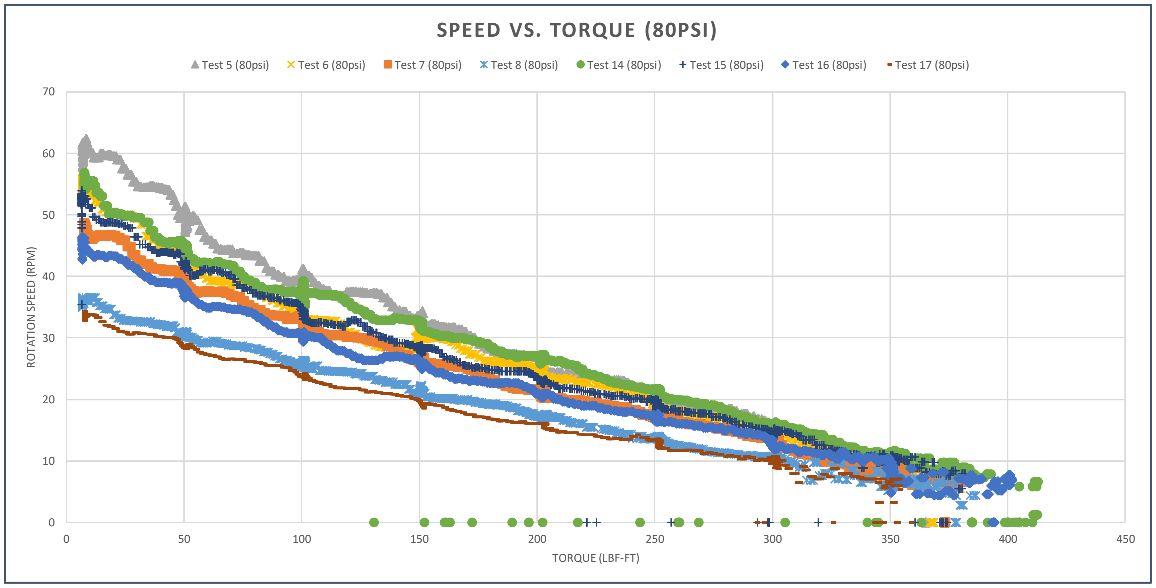

Figure 15(b): Sample dynamometer results for microhole downhole motor: 80 psi (~550 kPa) inlet pressure.

Volumetric flow rates ranged from ~20 to 50 scfm (~0.6 to ~1.4 m^3/min). The stall torque was lower than expected because of choked flow in the air supply line. A larger compressor and/or supply line are needed to reach the predicted stall torque. Tests were also conducted at the Sandia HOT drilling facility under more realistic drilling conditions. These tests were conducted with a 3 in. (~7.6 cm) percussive hammer attached to the end of the motor. Compressed air from an external compressor drove the motor and hammer. Two 24 in. (~61 cm) drilling tests were conducted on the Sierra White granite block, and afterward, the internal motor components showed no signs of accelerated wear or damage.

Weight-on-bit and Torque Management

Drilling systems that use downhole rotation must react torque either through the drill string or near the motor to achieve effective drilling performance. Problems with drill string loading, such as buckling, friction, and twist, become more severe as borehole diameter decreases. Therefore, for small boreholes, it is preferable to react torque downhole without interfering with the application of WOB. Figure 16 shows the design of the torque reaction mechanism, which has two or more linkages (n) that transmit vertical forces to the borehole. The net radial force, F_r, is the scalar sum of the force across all linkages. In our analysis, we assumed the revolute joints are frictionless and the system is quasi-static (not accelerating). We also assumed the applied loads are far larger than any internal gravitational loads on the links/wheels. The applied force $F_{in,z}$ is controlled via the drilling rig, and $F_{out,z}$ is the actual WOB.

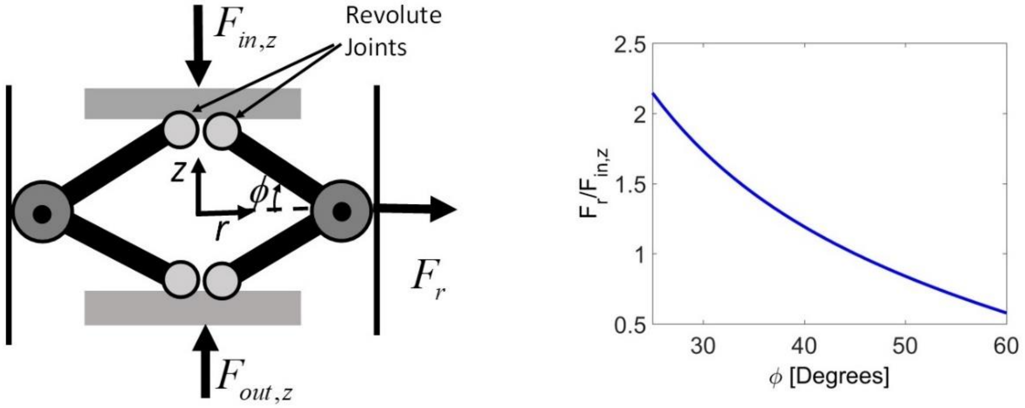

(a) Schematic Diagram

(b) Variable Force Ratio

Figure 16: Schematic diagram illustrating the torque reaction mechanism design (a) and a plot of the predicted output force ratio as a function of the engagement angle, φ (b).

The equation for the radial force, F_r, is given by Equation (4).

$$F_r = \sum_{i=1}^{n} \frac{1}{n} \frac{F_{in,z}}{\tan \phi} = \frac{F_{in,z}}{\tan \phi} \qquad \text{Eq. 4}$$

When the applied force, $F_{in,z}$, is relatively low, the mechanical advantage becomes relevant. Figure 17 shows that when the wheels contact the borehole wall, these radial forces act as normal forces for friction in the *z* and θ directions. The net radial force, F_r, can be used to find the net vertical friction force, $F_{f,z}$, Equation (5), and the net tangential friction force, $F_{f,\theta}$, Equation (6). All net forces are scalar quantities.

$$F_{f,z} = F_r \mu_z \qquad \text{Eq. 5}$$

$$F_{f,\theta} = F_r \mu_\theta \qquad \text{Eq. 6}$$

The tangential friction force, $F_{f,\theta}$, reacts the torque from the downhole motor, and the translational friction force, $F_{f,z}$, resists the transmission of force from $F_{in,z}$ to $F_{out,z}$. A force and torque balance analysis of the mechanism produces Equations (7) and (8). We use the variables, μ_z and μ_θ, to represent the coefficients of friction for motions in the axial and tangential directions, respectively.

$$\tau_{in} \leq \frac{F_{in,z}}{tan\,\phi} \frac{D}{2} \mu_\theta \qquad \text{Eq. 7}$$

$$F_{out,z} = F_{in,z} - \frac{F_{in,z}}{tan\,\phi} \mu_z \qquad \text{Eq. 8}$$

The design objective is $\mu_z << \mu_\theta$ to effectively transmit WOB to the bit while also reacting torque. A rolling contact may be used to enable this direction-dependent behavior. The wheels shown in Figure 17 use rolling contact to move in the z direction but sliding motion to move in the θ direction. With this design, μ_θ can be tailored to be about an order of magnitude larger than μ_z.

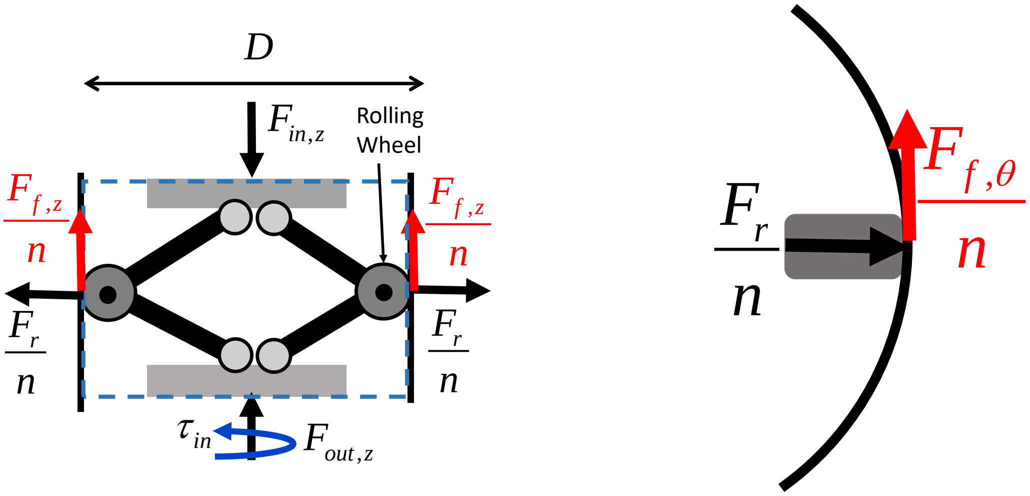

(a) Side View (b) Top View

Figure 17: Diagrams illustrating directionally dependent behavior through rolling elements.

With low rolling friction, μ_z, favorable scaling can be achieved using multiple modules in series as shown in Figure 18, enabling increased torque reaction and robustness with only small reductions in output force, $F_{out,z}$. As long as μ_z is small (e.g., 0.1), most of the vertical force will be transmitted to the next module. Each set of rollers pushes out with slightly reduced radial force. For multiple modules, $F_{in,z}$ is still applied at the top, but $F_{out,z}$ is the output force through all modules, and the tangential friction force, $F_{f,\theta}$, is the net force associated with all modules. The performance of a system with N modules is predicted by Equations (9) and (10).

$$F_{out,z} = F_{in,z}\left(1 - \frac{\mu_z}{\tan\phi}\right)^N$$ Eq. 9

$$F_{f,\theta} = \sum_{i=1}^{N} \frac{\mu_\theta F_{in,z}}{\tan\phi}\left(1 - \frac{\mu_z}{\tan\phi}\right)^{i-1}$$ Eq. 10

The torque needed to induce the start of slipping, τ_{slip}, can be computed via Equation (11) from the net tangential friction force.

$$\tau_{slip} = \frac{F_{f,\theta} D}{2} \qquad \text{Eq. 11}$$

Figure 18(b) shows how the normalized predicted input force, $F_{in,z}$, and slip torque, τ_{slip}, scale with multiple modules. Coefficients of friction are 0.1 and 1 for μ_z and μ_θ, respectively. The plot illustrates how the torque reaction capacity increases at a far faster rate than the applied load. Multiple modules also produce better performance in boreholes with deviations or blowouts. Multiple modules spaced apart can still react torque even if a single module does not perform well due to local problems in the borehole.

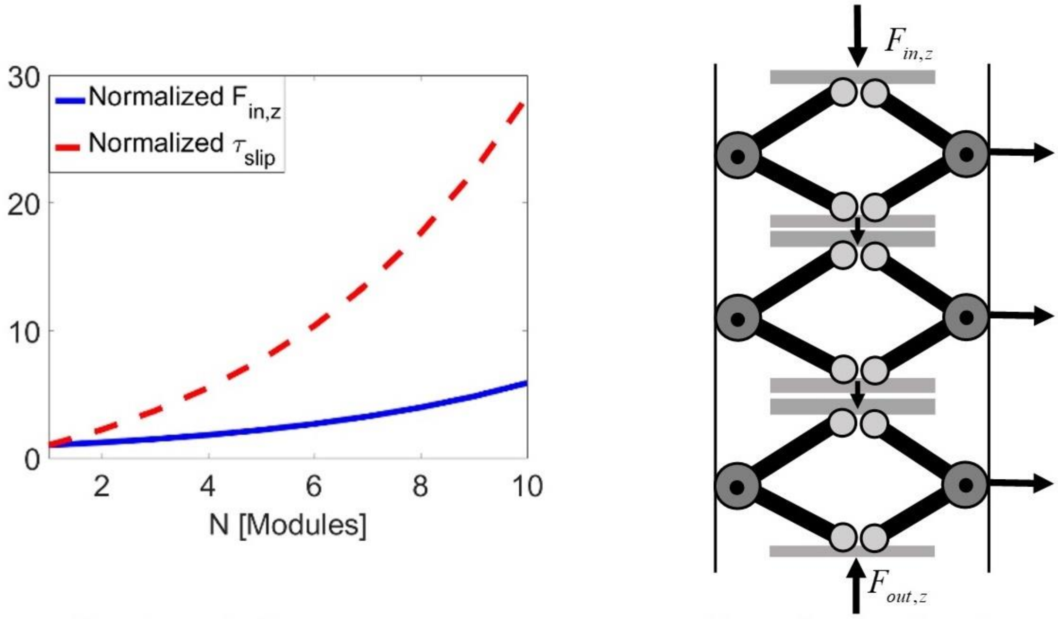

(a) Schematic diagram

(b) Predicted scaling plot

Figure 18: Schematic diagram (a) and predicted scaling plot (b) illustrating how multiple modules can be combined in series for improved torque reaction performance.

The torque reaction capacity, τ_{in}, and downhole WOB, F_{out}, are both proportional to the force applied at the top, F_{in}, which is true even when multiple modules are used. This allows the performance and downhole WOB to be controlled by modulating loads at the top by pulling up on the weight above the BHA, and the reaction torque capacity can be increased by increasing the WOB. This works well since torque and WOB generally scale together during drilling, but there could be conditions where we want to drill with high torque and modest WOB. This requires a small value of ϕ or a separate actuator to create an additional internal force in the module without impacting WOB.

A prototype (see Figure 19) was designed and evaluated in the laboratory and tested in a controlled field test. All components were made of alloy steel with plastic bushings. Post-test inspection revealed durability issues with the plastic bushings, and they were subsequently replaced with metal bushings for the remaining tests. Thrust loads were managed using high load thrust washers (shown in green in Figure 19), which were needed because the wheels had to roll while be subjected to large thrust loads from the downhole motor moment. We focused primarily on smooth wheels with a radius to match the borehole (Figure 19-b), minimizing wear.

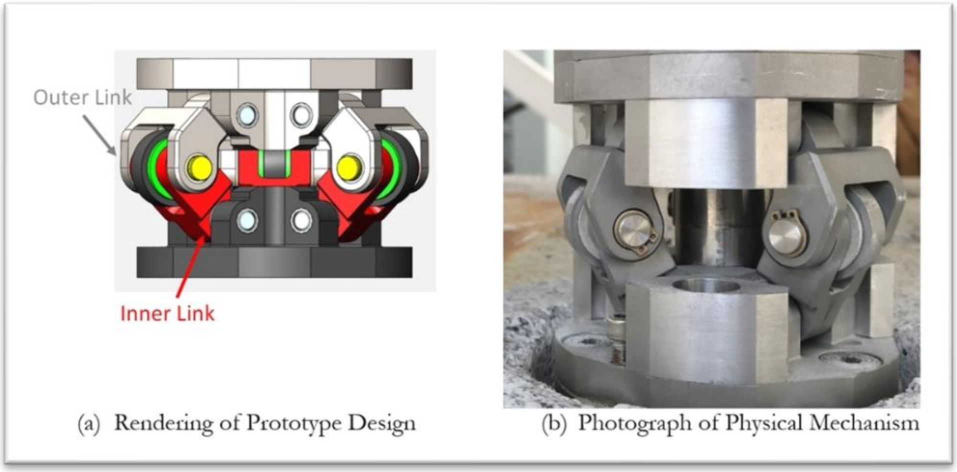

(a) Rendering of Prototype Design
(b) Photograph of Physical Mechanism

Figure 19: Rendering (a) and photograph (b) of the prototype design.

We constructed a laboratory testbed focused on dynamically evaluating torque reaction and WOB transmission to validate our models. This Dynamic Torque Reaction Simulator (see Figure 20) is part of Sandia's geothermal engineering facilities and is designed to emulate the physics of vertical WOB transmission and torque reaction. Figure 20(a) shows how the torque reaction mechanism sits within a rock sample. Weights are placed above the mechanism to simulate the use of drill collars to create downhole WOB. Axial forces and torques can be measured with each of the two force/torque sensors. Force/torque sensor 2 is connected to a pneumatic motor to impart torques onto the torque reaction mechanism. The thrust bearing above force/torque sensor 1 allows the system to rotate if the torque reaction mechanism slips. The rotary position of the torque reaction mechanism and pneumatic motor can be measured using a US Digital® MAE3 encoder system (not shown). Finally, a linear actuator is used to move the whole assembly up or down (like in real drilling) with measurements of both above-hole and downhole forces and torques.

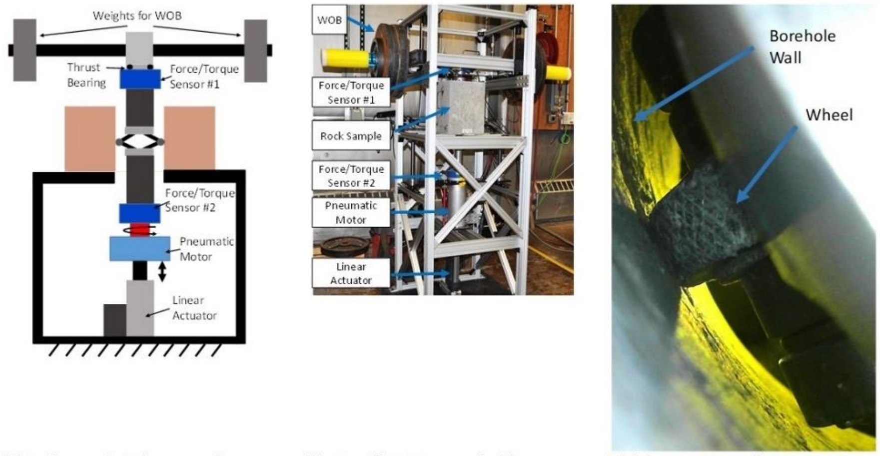

(a) Schematic Diagram for a Torque Reaction Testbed

(b) Sandia's Dynamic Torque Reaction Simulator

(c) Torque Reaction Mechanism Deployed in Sample Borehole

Figure 20: Sandia's Dynamic Torque Reaction Simulator.

Initial tests used one module and later tests used two modules. In each test, the mechanism was moved to the top of the block placing a set amount of weights and the linear actuator was then moved downward while increasing torques. The initial torque was slightly below the slip torque. Because the pneumatic motor does not act as an ideal torque source, the applied torque fluctuates. A typical set of experimental data is shown in Figure 21. Initially the rotation angle, θ, remains flat and then sharply increases as the torque approaches slip levels. Since the torque fluctuates, slipping often stops when the torque relaxes. Slipping is denoted with the black dashed line.

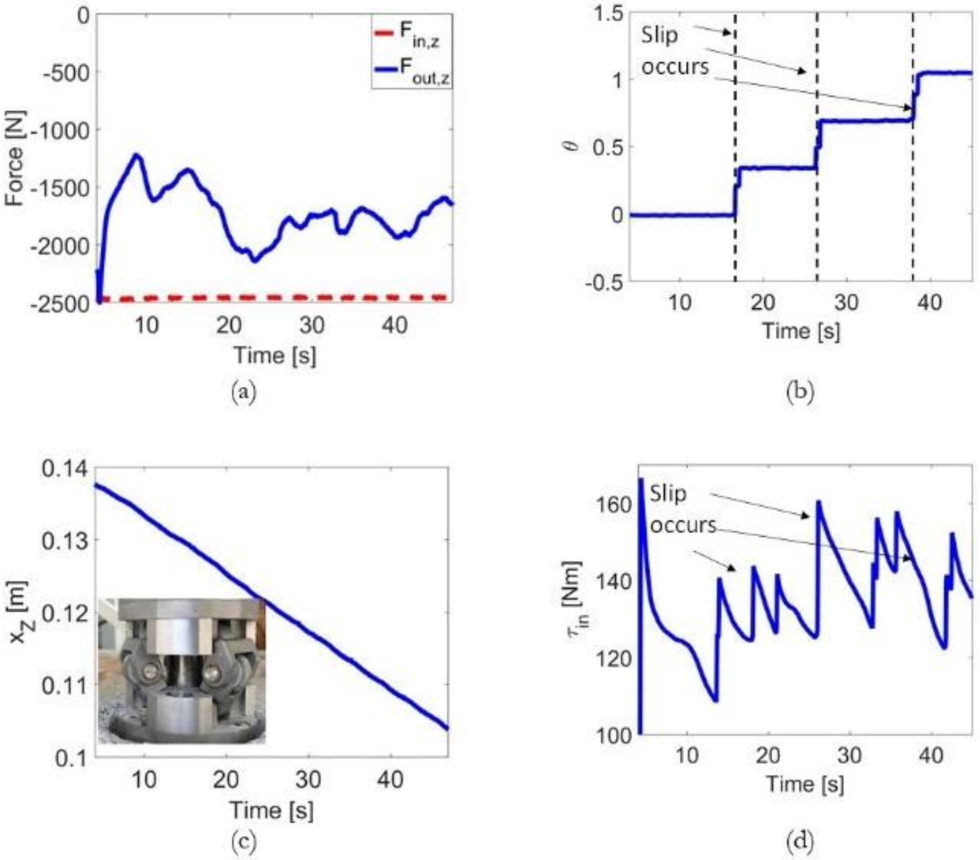

Figure 21: Experimental data showing z forces (a), measured rotation angle (b), linear displacement (c), and measured torque (d) during a trial in concrete with one module and 2,537 N (570 lbf) applied at top.

The amount of weight added to the top of the system was 2,136 N (480 lbf), and the other components weighed 400 N (90 lbf), resulting in a total applied force of 2,537 N (570 lbf). The measured forces in the z direction, using both force/torque sensors, are shown in Figure 21(a). The input force measured by force/torque sensor 1 are relatively constant and matched our estimate for total applied force ($F_{in,z}$). The force measured by force/torque sensor 2 is the force transmitted through our torque reaction mechanism ($F_{out,z}$) and is representative of the downhole WOB. As Figure 21 shows, while this force fluctuates as the mechanism moves downwards, the average force for this trial was within a 28% deviation of the input force. It is hypothesized that many of the fluctuations stem from irregular surfaces in the concrete borehole because the downhole WOB tracks within variations typical of drilling, despite the fact the mechanism is simultaneously moving downwards (Figure 21-c) and subjected to substantial twisting torques.

The torque applied by the pneumatic motor (Figure 21-d) was increased until frequent slipping occurred (Figure 21-b), which showed the measured rotation angle, θ. This is a highly dynamic process that depends on friction and involves the transition from static conditions to motion. Thus, slipping does not occur at consistent torque levels, and the slip torque threshold, τ_{slip}, is estimated using a statistical approach based on aggregate data for each trial. The angular velocity, $\dot{\theta}$, is first filtered to reduce effects of sensor quantization. Instances where nonzero $\dot{\theta}$ occur are recorded along with the corresponding measured "motion torque," which are compiled and sorted. We used the median value from lowest 10 motion torque points (bottom quartile of data) to determine the actual slip threshold, which is conservative because it uses the lowest slip levels.

Validation experiments were performed at the Sandia HOT percussive drilling facility simulating downhole geothermal conditions (Figure 22) using two modules. The test protocol involved spinning the motor with a nominal torque output (∼312 Nm) and then steadily increasing the applied axial force, $F_{in,z}$, until the spinning was completely halted by torque reacted by the module.

(a) Sandia HOT drilling facility

(b) Percussive hammer with two torque reaction modules

Figure 22: Sandia HOT facility (a) and percussive drill equipped with torque reaction modules (b).

The experiment was conducted with and without hammering (Figure 23). The results show that once a certain threshold WOB is reached, the rotation angle (blue line) stops increasing. The axial force to react the torque was ~40% greater with hammering than without, most likely due to the vibrations creating a dither-like effect that prevents static friction from building up. This is an important consideration for field drilling.

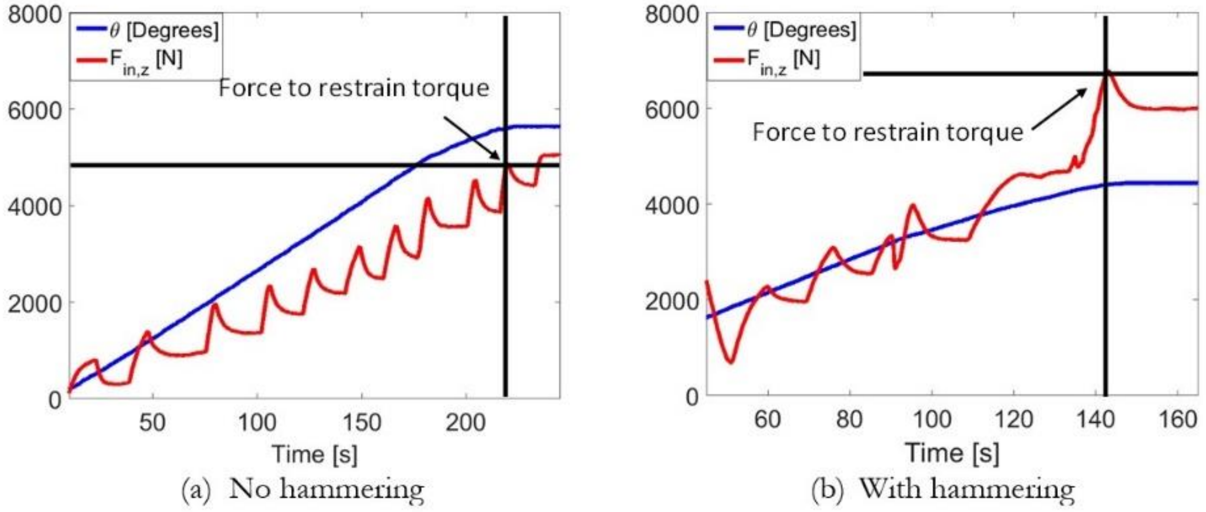

(a) No hammering (b) With hammering

Figure 23: Experimental data illustrating torque reaction (~312 Nm) without (a) and with (b) hammering.

Two options for dealing with this effect are adding more modules or increasing the applied force, $F_{in,z}$. Based on the limited HOT data, we anticipate that a percussive system with four modules will provide ~450 Nm (300 lbf-ft) of torque reaction while achieving a downhole WOB of ~2,200 N (500 lbf). During testing at the HOT facility, the module was exposed to torques of up to ~500 Nm and applied loads of ~160,000 N (3,600 lbf). The modules survived these loads without visible damage other than slight wear on the wheels and cracking of the plastic bushings. All plastic components were replaced with metal ones in future systems and experiments.

Limited Field Testing

Our field program focused largely on identifying gaps between existing COTS hardware and the requirements of the low WOB microhole drilling system. The percussive hammers used were COTS or lightly modified COTS components, providing a quicker path towards commercial adoption. Preliminary tests at the Sandia HOT facility used the COP 20 DTHH with a 3 in. (~7.6 cm) bit to assess the performance of the small-diameter valveless foot design. The tests used an external 175 psi (~1,200 kPa) compressor. Sierra White granite (unconfined compressive strength of 22 ksi [~150 kPa]) was used for the tests. Problems with the COP 20 hammer led us to adopt the QLX 35 based on its performance characteristics and size.

We developed a WOB management algorithm to optimize WOB during drilling. In conventional rotary drilling, increasing WOB results in a proportional increase in ROP. However, with percussive drilling, this is not necessarily the case. Our experience with percussive hammers has shown that continually increasing WOB does not lead to higher ROP. This has been shown in the literature, as well—Song et al. (2020) demonstrated that increasing WOB does not lead to higher ROP in percussive drilling (unlike in rotary drilling). There is a sweet spot in the ROP/WOB relationship that does not exist at maximum WOB.

We implemented an optimization algorithm—called a golden section search (GSS)—to systematically identify the preferred WOB for a given set of conditions. The GSS algorithm assumes that the global extrema lie within a search interval (a,b) and that the objective function is unimodal between (a,b) (Kiefer, 1993). The space is sequentially searched with decreasing intervals based on the golden ratio. This approach is well suited for ROP optimization because the limits (a,b) may be determined analytically using the Hustrulid and Fairhurst (1971) physics model for percussive drilling, which defines the bounds of drilling phases based on parameters of the drilling medium and the drilling process. The GSS algorithm can then be performed within this smaller interval.

The results of the WOB optimization algorithm implementation (see Figure 24) show the maximum ROP is achieved at an intermediate level of WOB. This optimized value would likely be missed using the standard WOB step test (incremental increases in WOB) used in rotary drilling.

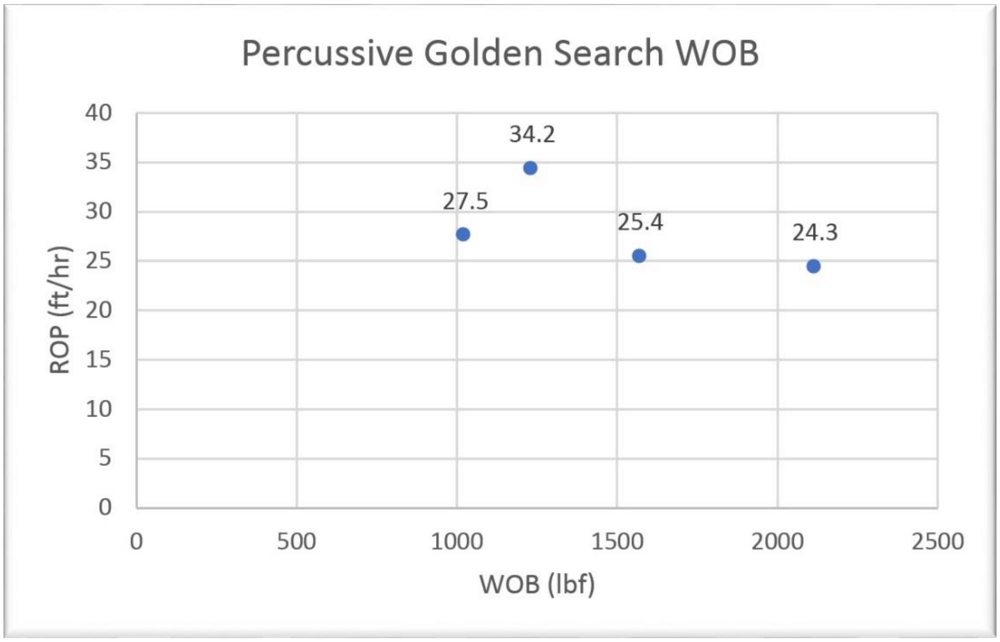

Figure 24: WOB control optimization algorithm results.

A drill-off test (man versus machine) was conducted to compare the results of the optimization algorithm versus a static WOB setpoint. For the comparison, the same hammer was used to drill 39 in. (~1 m) using external compressed air set at 175 psi (~1,200 kPa). The static WOB setpoint was 4,000 lbf (~18,000 N). The machine WOB executed the GSS algorithm described previously. The results of the test showed a nearly 20% improvement in ROP (27 ft/hr vs. 33 ft/hr [~8 m/hr vs. ~10 m/hr]) using the GSS-optimized WOB selection versus the static value.

The Blue Canyon Dome site at the New Mexico Tech Energetic Materials Research and Testing Center in Socorro, New Mexico, was used for additional field tests. The formation consists of weathered rhyolite containing large clasts in the uppermost 30 to 35 ft (~9.1–10.7 m). Deeper in the formation, unweathered rhyolite extends to a depth of up to 400 ft (~122 m). The unconfined compressive strength of the rock is ~38 ksi (~260 MPa).

The drill pipe conveyance system was designed to (i) provide up to 2,000 lbf (~8,900 N) drilling force, (ii) generate and handle 4,000 lbf (~17,800 N) of pullback force, (iii) provide up to 150 ft (~9.1 m) of continuous drilling, and (iv) traverse up to 3 in./s (7.6 cm/s) during drilling and pullback. The BHA was designed to drill holes up to 4.0 in. (10.2 cm) diameter.

A borehole was spudded and cased to 35 ft (~10.7 m) with 5.625 in. OD x 4.25 in. ID casing. An additional 20 ft (~6 m) of 4 in. (~10 cm) hole was left open. The overall drilling system configuration is shown in Figure 25. A wireline truck was used to deploy the drilling assembly and regulate the WOB by either pulling back or lowering the drilling assembly. A load cell on the main pulley measures the hook load, and a hose reel at the surface provides the conduit for compressed air that powers the downhole motor and percussive hammer. The wireline truck controls could be operated either manually or with a joystick (computer).

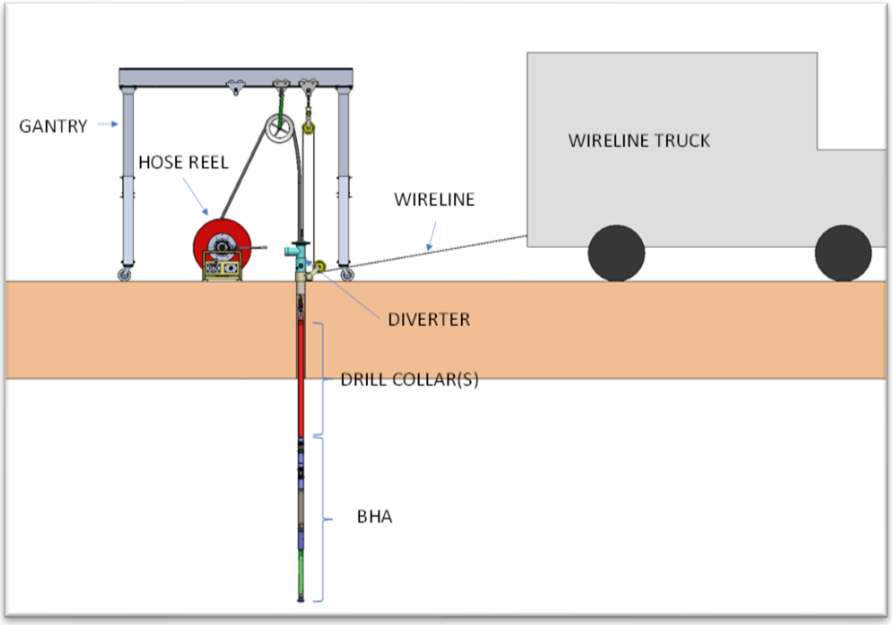

Figure 25: Drilling System Configuration.

Each drill collar was 6 ft (~1.8 m) long and weighed ~180 lb (~81.6 kg) and was stacked to achieve the desired maximum WOB. Intermediate WOB was regulated through the wireline pullback. The BHA consisted of the percussive DTHH, downhole motor, and the WOB/torque reaction modules. A 200 psi (~1,380 kPa), 400 scfm (~11.3 m^3/min) air compressor powered the drilling assembly for this field test. An electro-pneumatic ball valve was used to control the flow of air from the compressor to the hose reel. Table 1 lists the individual drilling assembly components. For the initial tests, only five drill collars were used due to the spudded hole depth. The load cell values listed in the table represent twice the WOB load due to the pulley. The load at the bit was no more than half the load cell reading due to friction and drag.

Four of the torque reaction modules were deployed as part of a complete microhole drilling system. This wireline-deployed system used a downhole motor and percussive hammer to drill 101.6 mm (4 in.) diameter holes. Drill collars were used to apply WOB. The BHA consisted of (from bottom to top) a percussive hammer, downhole motor, torque reaction modules, and up to 1,800 lb (~816 kg) of drill collars. When deployed during drilling, visual inspection was used to assess the performance of the torque reaction modules. The downhole motor caused the cable to twist when the torque reaction mechanism was not engaged with the formation.

Table 1: Drilling Assembly Components with Length and Load Cell Reading

BHA Number	Description	Length (in.)	Load Cell (lbf)
1	QLX35	35.25	
2	Shock Sub	14.19	
3	Air motor	37.68	450
4	WOB module 1	16.00	471
5	21 in. sub	21.00	
6	WOB module 2	16.00	670
7	Drill collar	72.00	965
8	Drill collar	72.00	1,320
9	Drill collar	72.00	1,680
10	Drill collar	72.00	1,990
11	Drill collar	72.00	2,370

The motor and percussive hammer performed well, but there were challenges with the design and durability of some of the components, which need to be addressed prior to future testing. For example, the torque reaction module links were found to be damaged during drilling. The damage occurred on several of the links in a similar fashion. In addition, the drill conveyance system, which advances the drill bit and retracts it on pullback, requires additional capacity for pullback. The motor and percussive hammer were well matched and performed well before the other components failed.

Photos of the microhole field drilling system are shown in Figures 26 and 27.

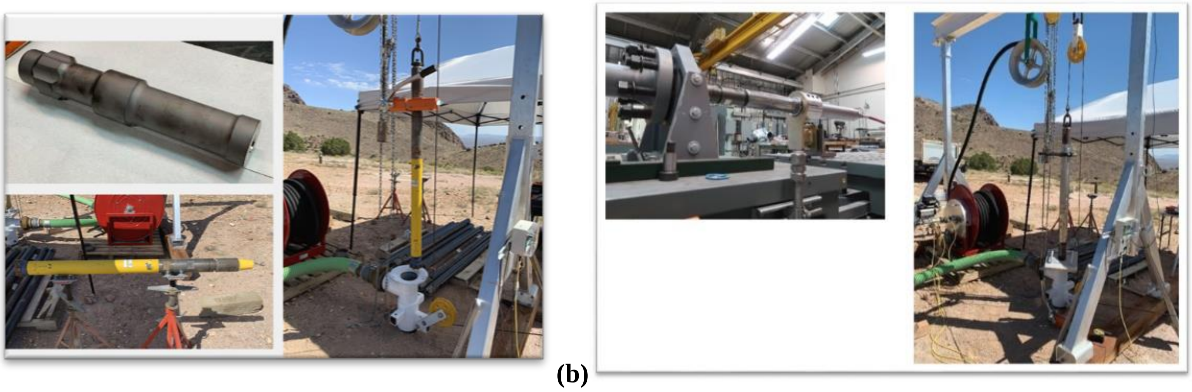

(a) **(b)**

Figure 26: Percussive hammer as assembled in the BHA(a) and air motor as assembled in the BHA (b).

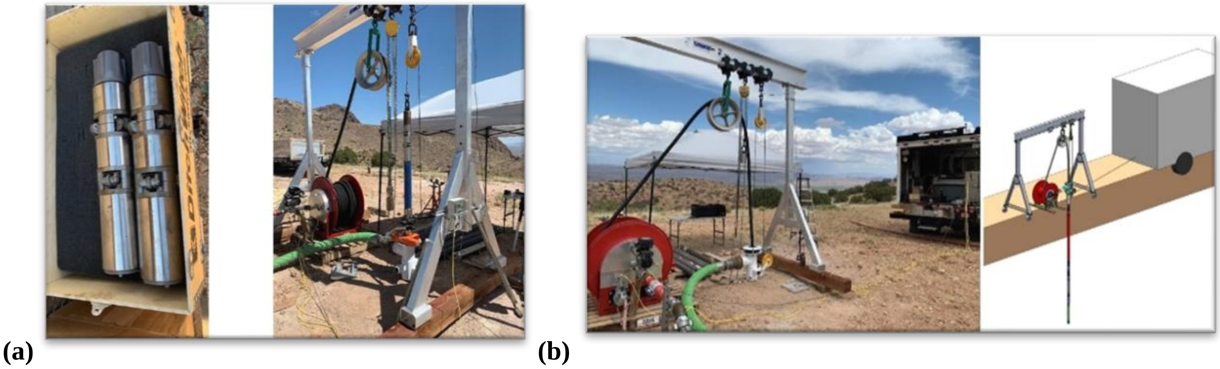

Figure 27: WOB modules (MADS) as built and assembled with two sets of reaction modules (a) and microhole system as built and as designed (b).

Conclusions

The results of our research into low WOB microhole drilling were very promising and could lead to lower cost drilling options during geothermal energy development. These technologies have broader application to other drilling systems requiring downhole rotation, such as directional drilling, which benefit from the ability to react torque near the motor rather than with the drill string. Similarly, the mechanical advantage principles can be used to create other types of relevant devices, such as inchworm type devices that lock within the borehole or cutting tools that exploit mechanical advantage to apply large radial loads to the borehole wall.

References

Albright, J.N., and D.S. Dreesen. (2000). Microhole technology lowers reservoir exploration, characterization costs. *Oil & Gas Journal*, 98(2): 39–41.

Finger, J.T., Combs, J., Goranson, C., Hockox C.E., Jacobsen R.D., and G. Polik. (1999). Slimhole Handbook: Procedures and Recommendations for Slimhole Drilling and Testing in Geothermal Exploration, SAND99-1976, Sandia National Laboratories, Albuquerque, New Mexico, October 1999.

Hustrulid, W.A., and Fairhurst, C. (1971). A theoretical and experimental study of the percussive drilling of rock part I—theory of percussive drilling. *International Journal of Rock Mechanics and Mining Sciences & Geomechanics Abstracts*, 8(4): 311–333.

Jeanloz, R., and H. Stone. (2013). Enhanced Geothermal Systems, JASON, JSR-13-320. The Mitre Corporation, McLean, Virginia, December 2013.

Kiefer, J. (1953). Sequential minimax search for a maximum, *Proc. Amer. Math.* Soc. 4:502–506.

National Energy Technology Laboratory. (2006). Microhole Technology: A Systems Approach to Mature Resource Development. DOE National Energy Technology Laboratory.

Randolph, S., J. Bosio, and B. Boyington. (1991). Slimhole Drilling: The Story So Far, *Oilfield Review*. pp. 46–54.

Song, X., Aamo, O.M., Kane, PA. et al. (2020). Influence of Weight-on-Bit on Percussive Drilling Performance. *Rock Mech Rock Eng*. https://doi.org/10.1007/s00603-020-02232-x

Zhu, T., and H.B. Carroll. (1995). Slimhole Drilling: Applications and Improvements, NIPER/BDM-0155. U.S. Department of Energy, Bartlesville, Oklahoma, August 1995.

Acknowledgments. The authors would like to thank Dennis Kaspereit of Geothermal Resources Group for the flow modeling effort. We would also like to thank Dennis King, Elton Wright, Joe Pope, Taylor Myers, and Josh Tafoya for helping with the field activities as well as the members of the EMRTC Blue Canyon Dome field site.

Funding Statement. This paper describes objective technical results and analysis. Any subjective views or opinions that might be expressed in the paper do not necessarily represent the views of the U.S. Department of Energy or the United States Government.

This work was supported by the U.S. Department of Energy Geothermal Technologies Program. Sandia National Laboratories, a multi-mission laboratory managed and operated by National Technology and Engineering Solutions of Sandia, LLC, a wholly owned subsidiary of Honeywell International, Inc., for the U.S. Department of Energy's National Nuclear Security Administration under contract DE-NA0003525.